Nano Research

ISSN 1998-0124 CN 11-5974/O4
https://doi.org/10.1007/s12274-020-2922-6

Research Article

Gate-tunable linear magnetoresistance in molybdenum disulfide field-effect transistors with graphene insertion layer

Hao Huang[1,§], Hongming Guan[2,§], Meng Su[1], Xiaoyue Zhang[2], Yuan Liu[3], Chuansheng Liu[1], Zhihong Zhang[2], Kaihui Liu[2], Lei Liao[1,3] (✉), and Ning Tang[2] (✉)

[1] *School of Physics and Technology, Wuhan University, Wuhan 430072, China*
[2] *State Key Laboratory of Artificial Microstructure and Mesoscopic Physics, School of Physics, Peking University, Beijing 100871, China*
[3] *Key Laboratory for Micro-/Nano-Optoelectronic Devices of Ministry of Education, School of Physics and Electronics, Hunan University, Changsha 410082, China*
[§] *Hao Huang and Hongming Guan contributed equally to this work.*

© Tsinghua University Press and Springer-Verlag GmbH Germany, part of Springer Nature 2020
Received: 10 February 2020 / **Revised:** 25 March 2020 / **Accepted:** 5 June 2020

ABSTRACT

Molybdenum disulfide (MoS_2) holds great promise as atomically thin two-dimensional (2D) semiconductor for future electronics and opto-electronics. In this report, we study the magnetoresistance (MR) of MoS_2 field-effect transistors (FETs) with graphene insertion layer at the contact interface. Owing to the unique device structure and high-quality contact interface, a gate-tunable linear MR up to 67% is observed at 2 K. By comparing with the MRs of graphene FETs and MoS_2 FETs with conventional metal contact, it is found that this unusual MR is most likely to be originated from the contact interfaces between graphene and MoS_2, and can be explained by the classical linear MR model caused by spatial fluctuation of carrier mobility. Our study demonstrates large MR responses in MoS_2-based systems through heterojunction design, shedding lights for the future magneto-electronics and van der Waals heterostructures.

KEYWORDS

molybdenum disulfide (MoS_2), contact, linear magnetoresistance, graphene insertion layer, mobility

1 Introduction

The magnetoresistance (MR) of a homogeneous semiconductor increases quadratically at low magnetic fields and saturates at high magnetic fields when magnetic field is larger than the inverse of the carrier mobility [1, 2]. However, many material systems were demonstrated to exhibit a linear MR under large magnetic fields without the sign of saturation, including silver chalcogenides, topological insulator, Dirac and Weyl semimetals et al. [3–12]. Theoretical models have been proposed to explain this unusual phenomenon, primarily including quantum and classical mechanisms [2, 13]. The quantum mechanism was first proposed by A. A. Abrikosov in 1998 to explain the unusual MR found in silver chalcogenides, which usually appears in the systematically gapless semiconductors with a linear energy spectrum system and low effective mass carriers [13–15]. Subsequently, M. M. Parish and P. B. Littlewood demonstrated another classical mechanism in 2003, known as the Parish–Littlewood (PL) model. Within disordered and inhomogeneous semiconductor, they pointed out the spatial fluctuation of carrier mobility is the main cause of the observed linear MR using a two-dimensional-random resistor network model [2, 16]. Subsequently, Kreutzbruck et al. demonstrated the correlation between the linear MR and the carrier mobility together with the crossover field from quadratic to linear, providing a reliable experimental support for the PL model [17]. Furthermore, by utilizing the Monte Carlo simulation, Kozlova et al. pointed out the multiple-electron scattering by the mobility-fluctuation islands is the microscopic nature of the classical linear MR [18]. The cycloidal motions of electrons tend to be deflected, giving rise to the resistance in proportion to the magnetic fields.

Two-dimensional (2D) semiconducting transition metal dichalcogenides (TMDCs) hold potentials for next-generation's electronic applications including logic devices, information storage, photodetector, as well as spin and valley-based electronics [19–24]. The electronic, photonic, and optoelectronic properties of TMDCs are well and widely studied [25–28], however, less experimental works have been focused on MR behaviors. Ye et al. demonstrated the few-layer MoS_2 exhibits the weak localization via the MR measurements and estimated the spin-orbit scattering length [29]. Jie et al. observed an MR ratio of −12.7% in MoS_2-$CoFe_2O_4$ heterostructure, which can be attributed to the spin accumulation and spin injection to the MoS_2 layers [30]. Such less work of MR is largely due to the moderate electrical performance of conventional metal-contact TMDC devices.

Recently, van der Waals (vdW) contacted field-effect transistors (FETs) with greatly improved electrical performance have been demonstrated [31–35]. Here, by taking advantage of these advances, we study the MR behavior of the MoS_2 FETs with a graphene insertion layer in the contact region (graphene-inserted MoS_2 FETs). Owing to the unique device structure and high-quality contact interface, a large gate-tunable positive linear MR up to 67% has been obtained at low temperature.

Address correspondence to Lei Liao, liaolei@whu.edu.cn; Ning Tang, ntang@pku.edu.cn

Through the comparisons with monolayer graphene FETs and MoS_2 FETs with conventional metal contact (pure MoS_2 FETs), it is found that the large linear MR comes from the contact interfaces between graphene and MoS_2, which can be explained by the classical PL model. Our study demonstrates large MR responses in MoS_2-based systems through heterojunction design, shedding lights for the future magneto-electronics and vdW heterostructures.

2 Experimental

The fabrication processes of MoS_2 FETs with graphene insertion layer are illustrated in Figs. 1(a)–1(f) (see the Method seciton for detailed methods). Briefly, the as-grown monolayer graphene film on Cu foil was first transferred on highly doped silicon (p^{++}) covered with 300 nm SiO_2 (Si/SiO_2) using wet transfer method (Fig. 1(a)). Secondly, standard electron beam lithography (EBL) followed by high vacuum metal evaporation was performed to achieve metallization (50 nm Au) (Fig. 1(b)). Subsequently, O_2 plasma was employed to etch the exposed graphene, leaving only the graphene underneath the Au electrodes (Fig. 1(c)). Then, polyvinyl alcohol (PVA) films were used to cover the electrodes on the Si/SiO_2 substrate, following with heating (70 °C) to ensure the Au/graphene electrodes can be peeled off from the Si/SiO_2 substrate with the PVA film (Fig. 1(d)). Next, the PVA film with Au/graphene electrodes was transferred to the pre-fabricated MoS_2 film on Si/SiO_2 substrate using a physical transfer system (Fig. 1(e)). In the end, the PVA film was removed by deionized water to complete the entire processes. Figure 1(f) demonstrates a schematic of a device structure and the cross-sectional view of the device is shown in Fig. 1(g). Figure 1(h) shows the atomic force microscope (AFM) image of the MoS_2 FETs, where the thickness of MoS_2 is measured as ~ 9 nm. The channel length and width are 2 and 1.6 μm, respectively. Raman spectroscopy was performed to determine the thickness of the chemical vapor deposition (CVD) grown graphene used in this work, as shown in Fig. 1(i). The peak of G band is lower than the 2D band, indicating that graphene is monolayer [36].

Electrical transport studies were carried out using variable temperature insert (VTI) with a superconducting magnet (Oxford instruments Inc.) and Keysight B2912A. Figure 2(a) shows the transfer characteristics (I_{ds}–V_{gs}) of the graphene-inserted MoS_2 FETs without magnetic field at room temperature and 2 K at both linear and logarithmic scales. An on-off ratio of > 10^7 can be observed at both room temperature and 2 K.

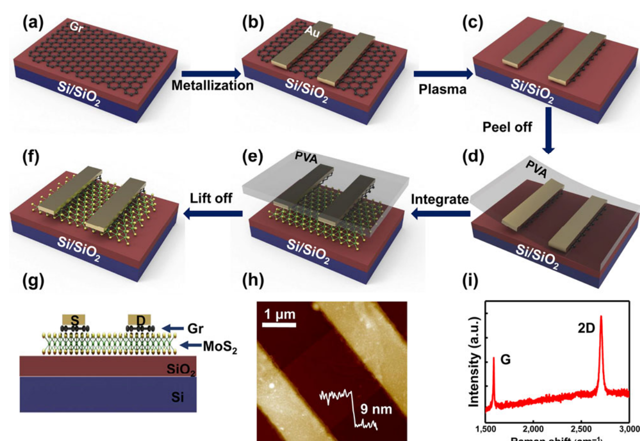

Figure 1 Device preparation process and characterization. (a)–(f) The fabrication processes of MoS_2 FETs with graphene insertion layer. (g) The cross-sectional view of the MoS_2 FETs. (h) The AFM image of the MoS_2 FETs. (i) The Raman Shift of the CVD-grown graphene.

The threshold voltage (V_{th}) shifts positively and the on-current increases along with the decrease of temperature, which are consistent with previous reports about MoS_2 with similar contacts [37]. The shifting of V_{th} can be traced back to the increase of the barrier at low gate voltage (V_{gs}) after decreasing the temperature; while the increase of on-current can be attributed to the decrease of the resistivity of MoS_2 channel due to the suppression of phonon scattering at low temperature [37–39]. In addition, a transition from insulating to metal further proves the high quality of MoS_2 channel and the non-damaging fabrication processes. The more intuitive differences between low temperature and room temperature can be observed in the output characteristic curves (I_{ds}–V_{ds}) in Figs. 2(b) and 2(c). The I_{ds}–V_{ds} shows essentially linear behavior at room temperature. However, the I_{ds}–V_{ds} shows slightly nonlinear behavior at 2 K, indicating the existence of a finite Schottky barrier, which is also consistent with previous reports [37]. The electrical characteristics of pure MoS_2 FETs are shown in Fig. S1 in the Electronic Supplementary Material (ESM). Clearly, the pure MoS_2 FETs have a more pronounced barrier and therefore exhibit worse performance than the devices with graphene insertion layer. The remarkable electrical characteristics of the graphene-inserted devices suggested the existence of high-quality contact interface and channel for electron transport, which lays a foundation for further research on the magneto-transports.

After the basic examination of electrical performance, an out-of-plane external magnetic field is applied (test temperature is 2 K unless specifically mentioned). Figure 3(a) shows the I_{ds}–V_{gs} of the graphene-inserted MoS_2 FETs with different magnetic fields at V_{ds} = 1 V at both linear and logarithmic scales. The on-state currents of the devices are significantly suppressed under a magnetic field and decreases with the increase of magnetic field, indicating the existence of positive MR. Figure 3(b) shows the 2D plot of MR versus magnetic field (Y axis) and V_{gs} (X axis), where the MR as a function of magnetic field is determined from the field-dependent resistance R_H as $\mathrm{MR}(H)=\frac{R_H - R_{H=0}}{R_{H=0}}\times 100\%$. It is found that the MR changes not only with the magnetic field, but also with the change of the V_{gs}. It should be noted that the MR does not increase monotonically with the increase of the gate voltage, but reaches the maximum value at about V_{gs} = 20 V. In addition, the relations between MR and V_{ds} are also investigated, as shown in Fig. 3(c). The gate voltage is fixed at V_{gs} = 20 V. The current of the device is also suppressed with increasing the magnetic field, and the MR reaches a maximum value of 67% at B = 8 T near V_{ds} = 0.6 V. It illustrates that the MR of graphene-inserted MoS_2 FETs can be modulated by both V_{gs} and V_{ds}.

Subsequently, we perform the MR measurements by varying the magnetic field continuously with fixed V_{gs} and V_{ds}. For convenience, V_{ds} is fixed at 1 V. Surprisingly, a non-saturation quasi- linear MR can be observed at V_{gs} = 20 V, as shown in Fig. 4(a), which has never been observed in MoS_2 or other 2H-phase TMDC systems. The same MR results are also observed under different V_{gs}, as shown in Fig. 4(b). The magnitude of the MR increases first and then decreases with increasing V_{gs} and reaches a maximum value at V_{gs} = 20 V. Similar results can also be obtained in another MoS_2 device with the same fabrication processes, as shown in Fig. S2 in the ESM. The observed MR has no sigh of saturation even at 14 T. In addition, temperature-dependent measurements are also conducted. Briefly, MR stays almost constant when the temperature is lower than 30 K, and it starts to decrease as the

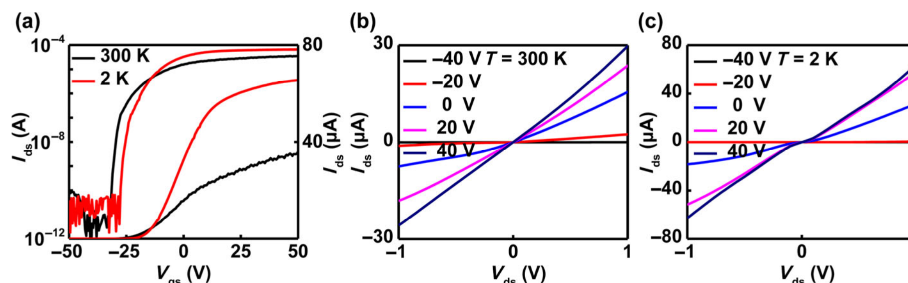

Figure 2 Electrical properties of graphene-inserted MoS_2 FETs without the magnetic field. (a) The I_{ds}–V_{gs} of the MoS_2 FETs at room temperature and 2 K at both linear and logarithmic scale. (b) and (c) The I_{ds}–V_{ds} of the MoS_2 FETs at room temperature and 2 K, respectively.

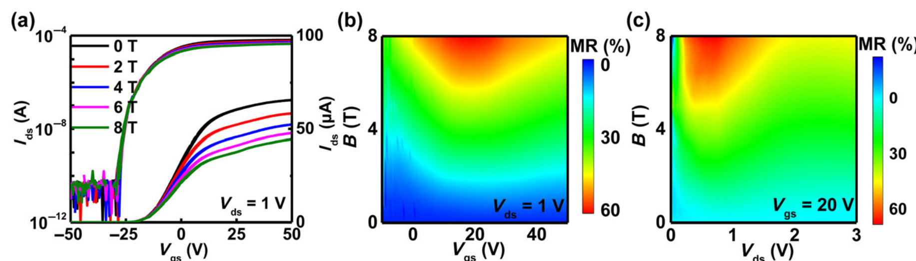

Figure 3 Electrical properties of graphene-inserted MoS_2 FETs under the magnetic field. (a) The I_{ds}–V_{gs} of the MoS_2 FETs with different magnetic field at V_{ds} = 1 V at both linear and logarithmic scale. (b) 2D plot of the MR of the MoS_2 FETs versus magnetic field (Y axis) and V_{gs} (X axis) extracted from I_{ds}–V_{gs} with different magnetic field. (c) 2D plot of MR versus magnetic field (Y axis) and V_{ds} (X axis) at V_{gs} = 20 V.

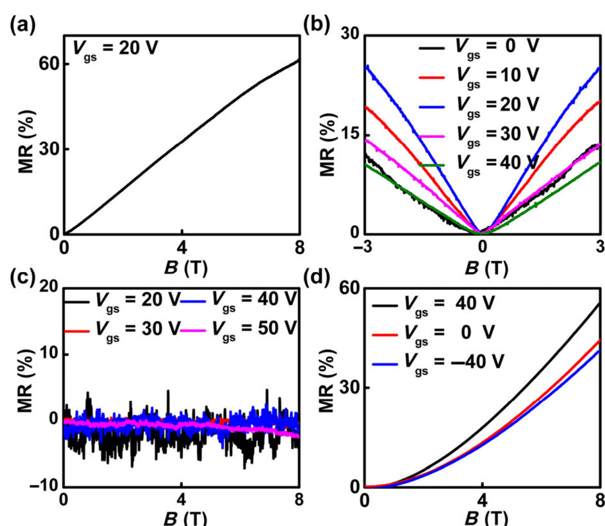

Figure 4 The MRs of three types devices at 2 K. (a) The MR of the MoS_2 FETs in the case of fixing V_{gs} with a varying magnetic field. (b) The MRs of the MoS_2 FETs under different V_{gs}. (c) The MRs of the pure MoS_2 FETs in the case of fixing V_{gs} with a varying magnetic field. (d) The MRs of the graphene FETs in the case of fixing V_{gs} with a varying magnetic field.

temperature reaches 77 K, and when the temperature exceeds 150 K, MR appears to saturate at high fields. This could be attributed to the phonon scattering which becomes the dominant scattering mechanism at higher temperature.

3 Discussion

In order to seek the origination of the observed linear MR, the magneto-transports of the pure MoS_2 transistors as well as the monolayer graphene FETs are also performed. Figures 4(c) and 4(d) show the MRs of the pure MoS_2 FETs and monolayer graphene FETs at 2 K (more information can be seen in Fig. S3 (pure MoS_2 FETs) and Fig. S4 (graphene FETs) in the ESM, respectively). It is obvious to see that no MR appears in pure MoS_2 FETs even at 8 T, while the graphene FETs exhibits a non-saturation linear MR response, which is of high similarity to the results of graphene-inserted MoS_2 FETs. Based on the above results, we can make an analysis for the linear MR in graphene-inserted MoS_2 FETs. A schematic of the disassembling of MR is shown in Fig. S5 in the ESM, or expressed by the following equation

$$R_{\text{total}} = 2(R_{\text{Au}} + R_{\text{Gra-Au}} + R_{\text{Gra}} + R_{\text{Gra-MoS}_2}) + R_{\text{MoS}_2}$$

where R_{Au} counts for the resistance of the Au electrode, R_{Gra-Au} the resistance of the interface between the Au electrode and graphene, R_{Gra} the resistance of the graphene, $R_{Gra-MoS_2}$ the resistance of the interface between graphene and MoS_2, and R_{MoS_2} represents the resistance of MoS_2. Clearly, R_{Au} and R_{Gra-Au} are quite small so that there is no influence to the resistance of the device. Moreover, according to the results of pure MoS_2 devices, R_{MoS_2} does not change under magnetic field, so it doesn't contribute to the linear MR of the whole device. Meanwhile, though a similar linear MR behavior up to 60% happens in pure graphene devices, the resistance of the graphene insertion layer is quite small, as low as several tens of Ohm [40]. So, the MR of the graphene insertion layer is not large enough to make any influence to R_{total}. Therefore, it can be speculated the linear MR behavior of the graphene-inserted MoS_2 FETs is most likely to come from the interface between graphene and MoS_2. The inserted graphene layer here acts like a chemical "catalyzer". Although graphene itself does not contribute to the linear MR of the whole device, the transport behavior of the electrons in graphene will be retained, and the linear MR is given rise when the electrons pass through the interface between graphene and MoS_2. The high-quality interface is the key to this, which sharply decreases the scattering of electrons with defects and interfacial charge trapping states [33], ensuring the transport behavior of electrons in graphene can be retained when they pass through the interface. The linear MR behavior is therefore observed.

For the physical mechanism, we begin the analysis from the MR of graphene. The observed linear MR in graphene can be attributed to the classical PL model due to the spatial charge inhomogeneity [8, 40, 41]. Similarly, for the linear MR in graphene-inserted MoS_2 FETs, it is very likely to be the same

mechanism. According to the PL model, it satisfies the following demands: The magnitude of the linear MR slope (the slope of the MR as a function of the magnetic field) is proportional to the magnitude of the mobility, and the crossover field from quadratic to linear is proportional to the reciprocal of the mobility [2, 16]. The relationship between the linear MR slope of graphene-inserted MoS_2 and the mobility of graphene-inserted MoS_2 together with the crossover field from quadratic to linear of graphene-inserted MoS_2 and the reciprocal of mobility of graphene-inserted MoS_2 are checked. Figures 5(a) and 5(b) exhibit the comparisons at different gate voltages. Since the MR is in high correlation with the graphene insertion layer, the comparison between the MR slope of graphene-inserted MoS_2 and the mobility of the graphene FETs together with the crossover field of graphene-inserted MoS_2 and the reciprocal of mobility of the graphene FETs are also conducted, as shown in Figs. 5(c) and 5(d). The mobilities are calculated according to the I_{ds}–V_{gs} curves of graphene-inserted MoS_2 FETs and pure graphene FETs. The mobility of graphene-inserted MoS_2 is dominated by the MoS_2 channel. According to the above analysis, the MoS_2 channel does not exhibit a linear MR behavior. So it's not surprising the MR slope and crossover field does not match the mobility of graphene-inserted MoS_2 FETs. However, the MR slope and crossover field do match with the mobility of the graphene FETs. Considering the close relation between the MR with the graphene insertion layer, it can be inferred this MR accords with the criterial of the classical PL model. The mobility of the graphene insertion layer changes with the gate, leading to the gate-tunable linear MR behavior.

In our devices, the graphene insertion layer is not completely covering on top of MoS_2, as shown in Fig. 1(h), therefore there exists in-plane velocity for electrons in graphene. Under the out-of-plane magnetic field, the in-plane cycloidal motions appear and simultaneously they are deflected by the multiple scattering processes around the mobility-fluctuation islands, giving rise to the linear MR in graphene. And it will be furtherly getting amplified at the interface, leading to the observed large linear MR of the graphene-inserted MoS_2 FETs. Considering solely on this interface, according to the results shown in the Fig. S6 in the ESM, the ratio between the interfacial and MoS_2 channel resistance is 1:6 at V_{gs} = 20 V. Thus, a giant "local MR" up to 400% can be obtained at the interfaces.

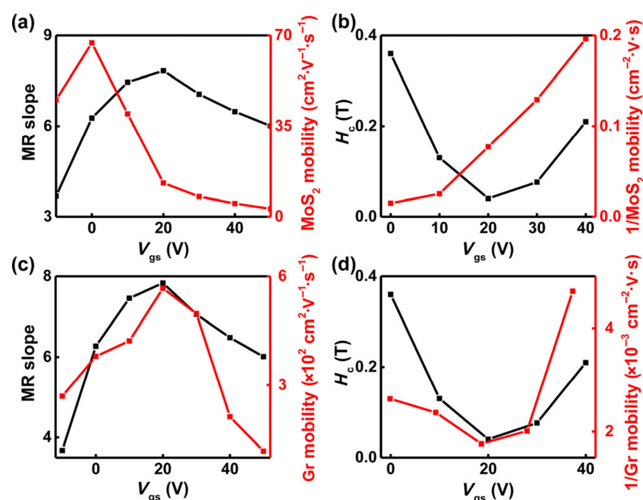

Figure 5 The verification of the PL model. (a) and (c) The MR slopes of the graphene-inserted MoS_2 FETs associate with the mobilities of graphene-inserted MoS_2 FETs and graphene insertion layer, respectively. (b) and (d) The crossover field of the graphene-inserted MoS_2 FETs versus the reciprocal of the mobilities of graphene-inserted MoS_2 FETs and graphene insertion layer, respectively.

4 Conclusion

In summary, graphene-inserted MoS_2 FETs with high-quality contact interface are constructed. A gate tunable non-saturation linear MR in graphene-inserted MoS_2 FETs has been obtained under an out-of-plane magnetic field. The MR reaches 67% at 2 K. By comparing with the results of graphene and pure MoS_2 FETs, it is found that the large linear MR is originated from the contact interface between graphene and MoS_2, and can be explained by the PL model. These results indicate that MoS_2-based devices could be used in the field of magnetic detections, opening up new possibilities for the research and developments of magnetic devices.

5 Method

5.1 Device fabrication

5.1.1 2D materials' wet transfer

The as-grown graphene film on Cu foil was spin-coated with polymethylmethacrylate (PMMA) at 2,000 rpm for 1 min and the back side is cleaned with O_2 plasma for 30 s. The Cu substrate was etched away by an aqueous solution of iron nitrate (0.05 $g \cdot mL^{-1}$) over 12 h and transferred into 10% HCl for 1 h. Finally, the film was washed with deionized water, then placed on Si/SiO_2 substrates, and dried at 90 °C. In the end, PMMA was removed by acetone.

5.1.2 Metallization

The Si/SiO_2 substrates covered with graphene were spin-coated with methyl methacrylate (MMA) and PMMA, and EBL (JEOL 6510 with Nanometer Pattern Generation System) was used to define the source and drain pattern. Metal contacts (50 nm Au) were then deposited using high vacuum evaporation.

5.1.3 Etching

O_2 plasma etch was used to remove the exposed 2D materials, leaving only 2D materials underneath the Au electrode.

5.1.4 Transfer

PVA film was used to cover the electrode on the Si/SiO_2 substrate and heated to 70 °C. The film was then peeled off from the Si/SiO_2 substrate. Next, the PVA film was transferred to the prepared MoS_2 flake on the Si/SiO_2 substrate using a physical transfer system. (The MoS_2 flake was mechanically exfoliated onto the Si/SiO_2 substrate by the scotch tape method.) In the end, the PVA was removed by deionized water.

5.2 Device characterization

Electrical transport studies were carried out using VTI with a superconducting magnet (Oxford instruments Inc.) and Keysight B2912A.

Acknowledgements

This work was supported by the National Key Research and Development Program of China (No. 2018YFB0406603), the National Natural Science Foundation of China (Nos. 61574006, 61522401, 61927806, 61521004, 11634002, and U1632156), as well as the Strategic Priority Research Program of Chinese Academy of Sciences (No. XDB30000000).

Electronic Supplementary Material: Supplementary material (the electrical properties of pure MoS_2 FETs without the magnetic field, the MRs of another graphene-inserted MoS_2 FETs sample, MRs of the pure MoS_2 FETs and monolayer graphene FETs at 2 K, the schematic of disassembling of the MR in the MoS_2 FETs with graphene insertion layer and the channel resistance and contact resistance of the graphene-inserted MoS_2 FETs) is available in the online version of this article at https://doi.org/10.1007/s12274-020-2922-6.

References

[1] Peierls, R. E. *Quantum Theory of Solids*; Clarendon Press, Oxford, 1955.

[2] Parish, M. M.; Littlewood, P. B. Non-saturating magnetoresistance in heavily disordered semiconductors. *Nature* **2003**, *426*, 162–165.

[3] Xu, R.; Husmann, A.; Rosenbaum, T. F.; Saboungi, M. L.; Enderby, J. E.; Littlewood, P. B. Large magnetoresistance in non-magnetic silver chalcogenides. *Nature* **1997**, *390*, 57–60.

[4] Lee, M.; Rosenbaum, T. F.; Saboungi, M. L.; Schnyders, H. S. Band-gap tuning and linear magnetoresistance in the silver chalcogenides. *Phys. Rev. Lett.* **2002**, *88*, 066602.

[5] Wang, C. M.; Lei, X. L. Linear magnetoresistance on the topological surface. *Phys. Rev. B* **2012**, *86*, 035442.

[6] Assaf, B. A.; Cardinal, T.; Wei, P.; Katmis, F.; Moodera, J. S.; Heiman, D. Linear magnetoresistance in topological insulator thin films: Quantum phase coherence effects at high temperatures. *Appl. Phys. Lett.* **2013**, *102*, 012102.

[7] Gusev, G. M.; Olshanetsky, E. B.; Kvon, Z. D.; Mikhailov, N. N.; Dvoretsky, S. A. Linear magnetoresistance in hgte quantum wells. *Phys. Rev. B* **2013**, *87*, 081311.

[8] Wang, W. J.; Gao, K. H.; Li, Z. Q.; Lin, T.; Li, J.; Yu, C.; Feng, Z. H. Classical linear magnetoresistance in epitaxial graphene on SiC. *Appl. Phys. Lett.* **2014**, *105*, 182102.

[9] Friedman, A. L.; Tedesco, J. L.; Campbell, P. M.; Culbertson, J. C.; Aifer, E.; Perkins, F. K.; Myers-Ward, R. L.; Hite, J. K.; Eddy, C. R. Jr.; Jernigan, G. G. et al. Quantum linear magnetoresistance in multilayer epitaxial graphene. *Nano Lett.* **2010**, *10*, 3962–3965.

[10] Narayanan, A.; Watson, M. D.; Blake, S. F.; Bruyant, N.; Drigo, L.; Chen, Y. L.; Prabhakaran, D.; Yan, B.; Felser, C.; Kong, T. et al. Linear magnetoresistance caused by mobility fluctuations in n-doped Cd_3As_2. *Phys. Rev. Lett.* **2015**, *114*, 117201.

[11] Novak, M.; Sasaki, S.; Segawa, K.; Ando, Y. Large linear magnetoresistance in the dirac semimetal TlBiSSe. *Phys. Rev. B* **2015**, *91*, 041203.

[12] Ali, M. N.; Xiong, J.; Flynn, S.; Tao, J.; Gibson, Q. D.; Schoop, L. M.; Liang, T.; Haldolaarachchige, N.; Hirschberger, M.; Ong, N. P. et al. Large, non-saturating magnetoresistance in WTe_2. *Nature* **2014**, *514*, 205–208.

[13] Abrikosov, A. A. Quantum magnetoresistance. *Phys. Rev. B* **1998**, *58*, 2788–2794.

[14] Abrikosov, A. A. Quantum linear magnetoresistance. *EPL Eur. Lett.* **2000**, *49*, 789–793.

[15] Abrikosov, A. A. Quantum magnetoresistance of layered semimetals. *Phys. Rev. B* **1999**, *60*, 4231–4234.

[16] Parish, M. M.; Littlewood, P. B. Classical magnetotransport of inhomogeneous conductors. *Phys. Rev. B* **2005**, *72*, 094417.

[17] von Kreutzbruck, M.; Lembke, G.; Mogwitz, B.; Korte, C.; Janek, J. Linear magnetoresistance in $Ag_{2+\delta}Se$ thin films. *Phys. Rev. B* **2009**, *79*, 035204.

[18] Kozlova, N. V.; Mori, N.; Makarovsky, O.; Eaves, L.; Zhuang, Q. D.; Krier, A.; Patanè, A. Linear magnetoresistance due to multiple-electron scattering by low-mobility islands in an inhomogeneous conductor. *Nat. Commun.* **2012**, *3*, 1097.

[19] Radisavljevic, B.; Radenovic, A.; Brivio, J.; Giacometti, V.; Kis, A. Single-layer MoS_2 transistors. *Nat. Nanotechnol.* **2011**, *6*, 147–150.

[20] Duan, X. D.; Wang, C.; Pan, A. L.; Yu, R. Q.; Duan, X. F. Two-dimensional transition metal dichalcogenides as atomically thin semiconductors: Opportunities and challenges. *Chem. Soc. Rev.* **2015**, *44*, 8859–8876.

[21] Franklin, A. D. Nanomaterials in transistors: From high-performance to thin-film applications. *Science* **2015**, *349*, aab2750.

[22] Ye, Y.; Xiao, J.; Wang, H. L.; Ye, Z. L.; Zhu, H. Y.; Zhao, M.; Wang, Y.; Zhao, J. H.; Yin, X. B.; Zhang, X. Electrical generation and control of the valley carriers in a monolayer transition metal dichalcogenide. *Nat. Nanotechnol.* **2016**, *11*, 598–602.

[23] Liang, S. H.; Yang, H. W.; Renucci, P.; Tao, B. S.; Laczkowski, P.; Mc-Murtry, S.; Wang, G.; Marie, X.; George, J. M.; Petit-Watelot, S. et al. Electrical spin injection and detection in molybdenum disulfide multilayer channel. *Nat. Commun.* **2017**, *8*, 14947.

[24] Mak, K. F.; McGill, K. L.; Park, J.; McEuen, P. L. The valley hall effect in MoS_2 transistors. *Science* **2014**, *344*, 1489–1492.

[25] Mak, K. F.; He, K. L.; Shan, J.; Heinz, T. F. Control of valley polarization in monolayer MoS_2 by optical helicity. *Nat. Nanotechnol.* **2012**, *7*, 494–498.

[26] Xu, X. D.; Yao, W.; Xiao, D.; Heinz, T. F. Spin and pseudospins in layered transition metal dichalcogenides. *Nat. Phys.* **2014**, *10*, 343–350.

[27] Guan, H. M.; Tang, N.; Huang, H.; Zhang, X. Y.; Su, M.; Liu, X. C.; Liao, L.; Ge, W. K.; Shen, B. Inversion symmetry breaking induced valley hall effect in multilayer WSe_2. *ACS Nano* **2019**, *13*, 9325–9331.

[28] Zeng, H. L.; Dai, J. F.; Yao, W.; Xiao, D.; Cui, X. D. Valley polarization in MoS_2 monolayers by optical pumping. *Nat. Nanotechnol.* **2012**, *7*, 490–493.

[29] Neal, A. T.; Liu, H.; Gu, J. J.; Ye, P. D. Magneto-transport in MoS_2: Phase coherence, spin-orbit scattering, and the hall factor. *ACS Nano* **2013**, *7*, 7077–7082.

[30] Jie, W. J.; Yang, Z. B.; Zhang, F.; Bai, G. X.; Leung, C. W.; Hao, J. H. Observation of room-temperature magnetoresistance in monolayer MoS_2 by ferromagnetic gating. *ACS Nano* **2017**, *11*, 6950–6958.

[31] Liu, Y.; Wu, H.; Cheng, H. C.; Yang, S.; Zhu, E. B.; He, Q. Y.; Ding, M. N.; Li, D. H.; Guo, J.; Weiss, N. O. et al. Toward barrier free contact to molybdenum disulfide using graphene electrodes. *Nano Lett.* **2015**, *15*, 3030–3034.

[32] Cui, X.; Lee, G. H.; Kim, Y. D.; Arefe, G.; Huang, P. Y.; Lee, C. H.; Chenet, D. A.; Zhang, X.; Wang, L.; Ye, F. et al. Multi-terminal transport measurements of MoS_2 using a van der waals hetero-structure device platform. *Nat. Nanotechnol.* **2015**, *10*, 534–540.

[33] Liu, Y.; Guo, J.; Zhu, E. B.; Liao, L.; Lee, S. J.; Ding, M. N.; Shakir, I.; Gambin, V.; Huang, Y.; Duan, X. F. Approaching the Schottky-Mott limit in van der Waals metal-semiconductor junctions. *Nature* **2018**, *557*, 696–700.

[34] Huang, H.; Liu, X. Q.; Liu, F.; Liu, C. S.; Liang, X. L.; Zhang, Z. H.; Liu, K. H.; Zhao, X. Z.; Liao, L. Comprehensive insights into effect of van der Waals contact on carbon nanotube network field-effect transistors. *Appl. Phys. Lett.* **2019**, *115*, 173503.

[35] Chai, Y.; Hazeghi, A.; Takei, K.; Chen, H. Y.; Chan, P. C. H.; Javey, A.; Wong, H. S. P. Low-resistance electrical contact to carbon nanotubes with graphitic interfacial layer. *IEEE Trans. Electron Dev.* **2012**, *59*, 12–19.

[36] Ferrari, A. C.; Meyer, J. C.; Scardaci, V.; Casiraghi, C.; Lazzeri, M.; Mauri, F.; Piscanec, S.; Jiang, D.; Novoselov, K. S.; Roth, S. et al. Raman spectrum of graphene and graphene layers. *Phys. Rev. Lett.* **2006**, *97*, 187401.

[37] Liu, Y.; Guo, J.; Wu, Y. C.; Zhu, E. B.; Weiss, N. O.; He, Q. Y.; Wu, H.; Cheng, H. C.; Xu, Y.; Shakir, I. et al. Pushing the performance limit of sub-100 nm molybdenum disulfide transistors. *Nano Lett.* **2016**, *16*, 6337–6342.

[38] Radisavljevic, B.; Kis, A. Mobility engineering and a metal-insulator transition in monolayer MoS_2. *Nat. Mater.* **2013**, *12*, 815–820.

[39] Wang, J. L.; Yao, Q.; Huang, C. W.; Zou, X. M.; Liao, L.; Chen, S. S.; Fan, Z. Y.; Zhang, K.; Wu, W.; Xiao, X. H. et al. High mobility MoS_2 transistor with low Schottky barrier contact by using atomic thick h-BN as a tunneling layer. *Adv. Mater.* **2016**, *28*, 8302–8308.

[40] Liao, Z. M.; Wu, H. C.; Kumar, S.; Duesberg, G. S.; Zhou, Y. B.; Cross, G. L. W.; Shvets, I. V.; Yu, D. P. Large magnetoresistance in few layer graphene stacks with current perpendicular to plane geometry. *Adv. Mater.* **2012**, *24*, 1862–1866.

[41] Zhou, Y. B.; Han, B. H.; Liao, Z. M.; Wu, H. C.; Yu, D. P. From positive to negative magnetoresistance in graphene with increasing disorder. *Appl. Phys. Lett.* **2011**, *98*, 222502.